JOURNAL OF AIRCRAFT
Vol. 46, No. 3, May–June 2009

Potential Panel and Time-Marching Free-Wake Coupling Analysis for Helicopter Rotor

Seong Yong Wie*
Korea Advanced Institute of Science and Technology, Daejeon 305-701, Republic of Korea
Seongkyu Lee†
Pennsylvania State University, University Park, Pennsylvania 16803
and
Duck Joo Lee‡
Korea Advanced Institute of Science and Technology, Daejeon 305-701, Republic of Korea

DOI: 10.2514/1.40001

A potential-based panel method coupled with advanced time-marching free-wake techniques is developed to achieve fast and accurate prediction for unsteady aerodynamics and wake dynamics of helicopter rotating blades. This coupling analysis is enabled by using the equivalence of the doublet-wake panels and the vortex filaments. The coupled panel method allows the inclusion of the self-induced velocity of curved vortex filaments and high-order time integration for the computation of wake convection. A parallel computation is applied to the wake convection for fast numerical calculation. The computation of the induced velocity from each vortex filament is parallelized and computed separately. The velocity-field integration technique is used to avoid numerical singularity during the interaction between the wake and blades. It is found that blade-pressure predictions and the wake roll-up agree well with the measured data for helicopter rotors, both in hover and forward flight. Tip-vortex pairing phenomena are also predicted and compared with the measured data.

Nomenclature

C_M	=	moment coefficient
C_p	=	pressure coefficient
C_T	=	thrust coefficient
f	=	parabolic blending function
G	=	Green function
R	=	blade radius
S_B	=	solid surface
S_W	=	wake surface
Γ	=	vortex-filament strength
μ	=	doublet potential strength
μ_S	=	Rosenhead cutoff variable
ϕ	=	velocity potential
Ω	=	angular velocity of rotor

I. Introduction

ROTOR wake prediction is a key element for an analysis of rotor loads, performance, vibration, and acoustics. Unsteady panel methods [1–4] have been widely used as an alternative to computational fluid dynamics or lifting-line methods for the prediction of aerodynamics and wake dynamics in rotorcraft applications, mainly because they involve simple and accurate computation. Although the unsteady panel method has been sufficiently matured to predict airloads on the blade, an accurate and fast prediction of the wake dynamics has yet to be fully achieved. In particular, the prediction of complex phenomena of rotor wake dynamics such as tip-vortex pairing requires an advanced unsteady panel method.

It is known that the free-wake method, which is based on a vortex filament for a representation of the wake, is a powerful approach to simulate the complex wake roll-up [5,6]. More details of the wake can be calculated using a time-marching free wake with a lifting-surface method. Using this free-wake and lifting-surface method, the vortex pairing mechanism was well predicted and the results were compared with experimental data [7]. However, the lifting-line and lifting-surface methods cannot consider airload effects of airfoil thickness. For this reason, a panel method is proposed for describing airfoil thickness, which can be adequately modeled by the panel method.

In the present paper, advanced techniques for the prediction of the wake roll-up developed in the time-marching free-wake method have been incorporated into the potential-based panel method through application of the equivalence of constant strength of doublet-wake panels and vortex-ring filaments to achieve an accurate prediction of both aerodynamics and wake dynamics. Ahmed and Vidjaja [8] used the equivalence of constant strength of doublet panels and vortex rings to replace the doublet-wake panels with vortex-ring wake filaments. In their method, however, variation of the doublet strength distribution was prescribed over the blade camber line. In the present paper, the doublet panels are distributed and represented well, both on the blade surface and the wake surface. The doublet-wake surface is changed to curved vortex filaments for distorted wake behavior. An advanced curved vortex-filament model is applied to predict wake motion, and parabolic blending in interpolation of the velocity field is used to avoid the numerical singularity problem. Another numerical treatment is also used to reduce numerical instability of the wake.

Predictions of aerodynamics and the wake roll-up in hover are generally less computationally demanding than their forward-flight counterparts, but considerable computational cost is required when a multiple-blade rotor is considered. Nevertheless, fast computation can be achieved through application of parallel computation of the rotor wake. The induced velocity of each vortex filament is calculated separately by using a message passing interface.

The theory of the potential-based panel method is discussed in Sec. II. The time-marching free-wake techniques and an approach to

Received 23 July 2008; revision received 6 September 2008; accepted for publication 7 September 2008.

*Ph.D. Candidate, School of Mechanical, Aerospace and Systems Engineering; wsy278@kaist.ac.kr.
†Ph.D. Candidate, Aerospace Engineering Department; sxl348@psu.edu.
‡Professor, School of Mechanical, Aerospace and Systems Engineering; djlee@kaist.ac.kr. Member AIAA.

incorporate these techniques into the panel method is described in Sec. III. Section IV presents the implementation of advanced numerical schemes and a discretization of the governing equation. In Sec. V, numerical results of the present method are compared with experimental data for helicopter rotors in hover and forward flight, with emphasis on prediction of the rotor wake roll-up and tip-vortex pairing. Finally, conclusions follow.

II. Boundary Integral Formulation for a Lifting Body

The potential-based unsteady doublet panel method is derived from the boundary integral formulation. The detailed procedure and associated equations for the boundary integral formulation (BIF) are described in [9].

The potential flow, which gives the foundation for the panel method, is based on an incompressible, inviscid, irrotational flow. Velocity is given by the gradient of the velocity potential:

$$\mathbf{v} = \nabla\phi \tag{1}$$

Combining Eq. (1) with the continuity equation provides the Laplace equation for the velocity potential in the outer region: that is,

$$\nabla^2\phi = 0 \text{ outside } S_B \tag{2}$$

The boundary condition for rigid surfaces requires the velocity component normal to the solid surface S_B to be zero:

$$\frac{\partial\phi}{\partial n} = \mathbf{v}_B \cdot \mathbf{n} \tag{3}$$

where $\mathbf{v}_B$ is the velocity of the point on body surface S_B, and $\mathbf{n}$ denotes an outward unit normal vector. Normally, $\mathbf{v}_B$ is prescribed a priori by the kinematics of the body. An infinity boundary condition requires that the flow distribution due to the body motion through the fluid diminishes far from the body:

$$\phi = \mathcal{O}(R^{-\alpha})(\alpha > 0) \tag{4}$$

This condition is automatically fulfilled by the solution of the panel method. By applying the free-space Green function in Eq. (2), the following integral equation for the potential ϕ at any point denoted by x_* can be obtained:

$$E(x_*)\phi(x_*) = \int_S \left(\frac{\partial\phi}{\partial n}G(x_*;x) - \phi\frac{\partial G(x_*;x)}{\partial n}\right)\mathrm{d}S \tag{5}$$

where S includes both the body surfaces and wake surfaces, which are expressed as S_B and S_W, respectively, for a lifting problem; $G(x_*;x)$ is the Green function, which is represented as $-1/(4\pi r)$, with r being the distance between x and x_*; and $E(x_*)$ is dependent on the location of the point x_* relative to the body surface S_B and is given as follows:

$$E(x_*) = \begin{cases} 1 & x_* \text{ outside } S_B \\ 1/2 & x_* \text{ on } S_B \\ 0 & x_* \text{ inside } S_B \end{cases} \tag{6}$$

To complete the problem for the lifting case, the wake surfaces S_W should be taken into account. Let the two sides of the surface S'_W surrounding the wake become infinitesimally close to the surface of the wake. In this process, the closed surface S'_W is replaced by the two sides of the wake surface S_W. In the limit, the second terms in the integral of Eq. (5) are

$$\int_{S'_W} \phi\frac{\partial G}{\partial n}\mathrm{d}S = \int_{S_W} \Delta\phi\frac{\partial G}{\partial n}\mathrm{d}S \tag{7}$$

and

$$\int_{S_B} \frac{\partial\phi}{\partial n}G\mathrm{d}S = \int_{S_B} \Delta\left(\frac{\partial\phi}{\partial n}\right)G\mathrm{d}S = 0 \tag{8}$$

where Δ indicates the difference between the upper and lower surfaces in the wake. The complete boundary integral equation including the closed body surface S_B and the open wake surface S_W is given as follows:

$$E(x_*)\phi(x_*) = \int_{S_B}\left(\frac{\partial\phi}{\partial n}G - \phi\frac{\partial G}{\partial n}\right)\mathrm{d}S - \int_{S_W}\Delta\phi\frac{\partial G}{\partial n}\mathrm{d}S \tag{9}$$

In Eq. (9), $\partial\phi/\partial n$ is given by the boundary condition on the body surfaces [see Eq. (3)]. If x_* approaches the body surfaces, $E(x_*)$ is zero and Eq. (9) leads to the boundary integral equation for the value $\phi(x_*)$, and a system described by a linear algebraic equation needs to be solved.

III. Wake Description

A. Convection of Doublet Wake and Vortex Filament

Wake shed from the trailing edge is described by a doublet surface. This approach, however, cannot consider distorted wake behavior during convection. To predict distorted wake convection, the doublet-wake surface is replaced by a vortex ring at each time. This provides a connection between the unsteady panel and the time-marching free-wake method. The equivalence of the doublet surface and vortex ring is formulated in Eq. (10):

$$\mathbf{V}_{\mathbf{wake}} = \nabla\phi = -\frac{\mu}{4\pi}\int_{S_W}\nabla\frac{z}{r^3}\mathrm{d}S = \frac{\Gamma}{4\pi}\int_C\frac{\mathrm{d}\boldsymbol{l}\times\mathbf{r}}{r^3} \tag{10}$$

where $r = [(x-x_0)^2 + (y-y_0)^2 + (z-z_0)^2]$, μ denotes the wake-potential difference $\Delta\phi$), C represents the curve bounding the panel, and Γ ($\Gamma = \mu$) is the circulation strength of a vortex filament along C. As shown in Eq. (10), the doublet-wake panel involves surface integration for the calculation of the induced velocity. However, a vortex filament can give a simple line integration. Replacement of the doublet-wake panels with vortex filaments provides not only a simplified analytic formulation but also less singular behavior with a magnitude of an order of 1 smaller than the velocity obtained by the doublet-wake panel. Using this vortex-filament velocity, the total convected velocity of the wake can be constructed. In Eq. (11), the total convected velocity of the wake is composed of the freestream, the body effect velocity, and the wake velocity:

$$\mathbf{V} = \mathbf{V}_\infty + \mathbf{V}_{\mathbf{body}} + \mathbf{V}_{\mathbf{wake}} \tag{11}$$

In Fig. 1, doublet potential panel and replaced vortex filaments are shown. The replaced vortex filament rings are used in the time-marching free-wake method, which is developed to represent wake convection.

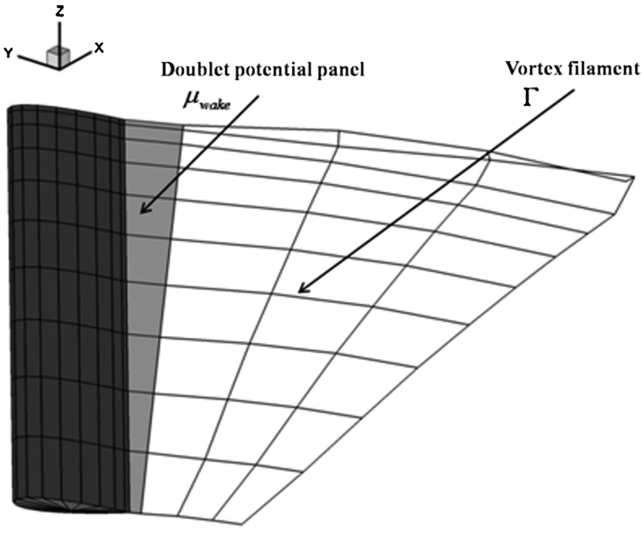

Fig. 1 Wake description using equivalence of doublet and vortex.

The replaced vortex-filament rings are used in the time-marching free-wake method, which is developed to represent wake convection. In the present free-wake method, the induced velocity of the wake on the collocation points on the blade and the wake surface is calculated or the wake roll-up is updated, because the velocity can be more easily and more accurately calculated by the vortex filaments than by the doublet panel. Another important advantage of representing the wake surfaces with the vortex filaments is that it provides easy implementation of techniques developed for the time-marching free-wake code: vortex-core modeling, inclusion of the self-induced velocity, and an advanced time-integration technique. In the present work, these techniques are coupled with the panel method to provide more accurate prediction of the wake dynamics. This coupling can improve the panel method in terms of not only the accuracy of aerodynamic load prediction, but also accurate prediction of the wake roll-up behavior.

IV. Numerical Implementation

A. Induced Velocity of a Curved Vortex Filament

Generally, vortex filaments are described as straight filaments. However, a vortex filament should be considered as a curved shape, because the rotor tip vortices and wake have a spiral motion. In addition, the curved vortex filament is useful to generate self-induced velocity, which is required for advanced description of wake movement. In this study, a parabolic blending function $f(\xi)$ is applied to the curved line interpolation. This parabolic blending interpolation can describe a circular line and provides a clear curved line without nonintuitive tangential vector to the line [10]. The parabolic blending function is given next:

$$f(\xi) = (1-\xi)p(r) + \xi q(s) \tag{12}$$

where ξ, r, and s indicate parametric variables, and $p(r)$ and $q(s)$ are parametric parabolas, which include the points P_1, P_2, P_3 and P_2, P_3, P_4. For a generalized parabolic blending function, the parametric variables r and s are nondimensionalized with specific length. Figure 2 shows the parabolic blending interpolation.

The induced velocity of the curved vortex line can be obtained from the Moore–Rosenhead equation:

$$\mathbf{V}_{\mathbf{ind}} = \frac{1}{4\pi}\int_C \frac{\mathbf{r}}{(|\mathbf{r}|^2+\mu_S^2)^{3/2}} \times \Gamma \frac{\partial y(\xi,t)}{\partial \xi} \mathrm{d}\xi \tag{13}$$

where $y(\xi, t)$ is the position on the curved line coordinate and μ_S is Rosenhead's cutoff variable for singularity removal. In the present work, the cutoff variable is set to be 10% of the chord length. These cutoff variables are based on the vortex-core model, which is correlated with the results of mathematical and experimental investigations [11].

This interpolation technique is only applied to the trailing vortex filament, which is perpendicular to the trailing edge. The shedding vortex filament, which is parallel to the trailing edge, is described by a straight filament, because distortion of the shedding part is less than that of the trailing part. From the trailing and shedding vortex filaments, the induced velocity field is constructed to describe the wake behavior.

B. Singularity Treatment During Interaction of Wake and Blade

In Fig. 3, the wake-potential panels interact with the blade at the advancing and retreating sides in forward flight. It could make a singular problem in the boundary integral formulation, because the wake approaches the blade surface or r equals 0. The wake potential is formulated in Eq. (7). Divergence of the potential value depends on the variable r, which indicates the distance between the wake and blade.

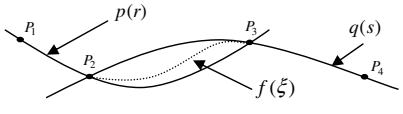

Fig. 2 Parabolic blending interpolation.

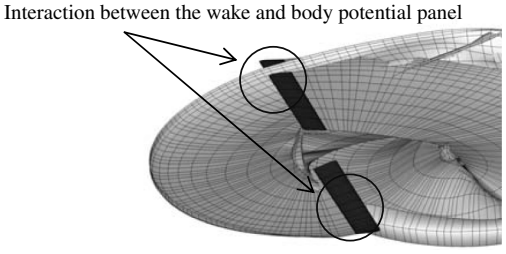

Fig. 3 Interaction between wake and body potential.

In the present work, a concept proposed by Gennaretti and Bernardini [12] to obtain the wake potential of vortex filaments without encountering the singularity problem is employed. In this approach, the wake potential is obtained indirectly through integration of the velocity field. Velocity induced by the doublet-wake surface is written as

$$\mathbf{V}_{\mathbf{wake}} = \nabla\left(\frac{1}{4\pi}\int_{S_W} \mu \frac{\partial}{\partial n}\left(\frac{1}{r}\right)\mathrm{d}S\right) \tag{14}$$

Using the equivalence of the doublet-wake surfaces and the vortex rings, Eq. (14) can be expressed as follows:

$$\mathbf{V}_{\mathbf{wake}} = \frac{\Gamma}{4\pi}\int_C \frac{\mathrm{d}\mathbf{l}\times\mathbf{r}}{r^3} \tag{15}$$

where $\Gamma = \mu$.

Although Eq. (15) also has a singularity when $r = 0$, the singularity can be overcome by using a vortex-core model such as those produced by Scully [13] and Vatistas et al. [14]. After obtaining the induced velocity at an arbitrary position, the wake potential can be determined through integration of the velocity along an arbitrary integral path:

$$\phi_{\mathrm{wake}} = \int_1^2 \left[\frac{\Gamma}{4\pi}\int_C \frac{\mathrm{d}\mathbf{l}\times\mathbf{r}}{r^3}\right]\cdot\mathbf{t}\,\mathrm{d}s \tag{16}$$

where $\mathbf{t}$ is the tangential vector to the integral path. The initial wake-potential value required in the velocity integration can be obtained from Eq. (7). Figure 4 shows this indirect velocity integral integration. This approach prevents the numerical singularity of the boundary integral formula. For this reason, this indirect approach is very useful in the blade–vortex interaction condition.

C. Predictor–Corrector Technique for Time Integration

For time integration of the wake convection, the predictor–corrector technique is applied to the free-wake method. New wake locations of the wake are determined by time integration as follows:

$$\mathbf{y}_{\mathbf{n+1}} = \mathbf{y}_{\mathbf{n}} + \int \mathbf{V}_{\mathbf{n}}\mathrm{d}t \tag{17}$$

where $\mathbf{n}$ is the time-step index, $\mathbf{y}$ denotes the location of the wake points, and $\mathbf{V}_{\mathbf{n}}$ is the local velocity at the n time step. High-order schemes for the time integration can be used to predict the wake trajectory, which is crucial to the prediction of aerodynamic loads,

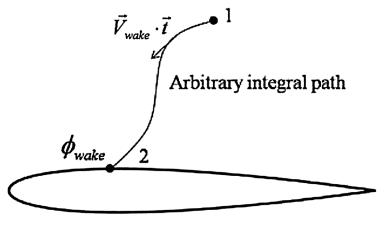

Fig. 4 Wake potential using velocity-field integration.

noise, vibration, and performance. In the present paper, the fourth-order Adams–Bashforth–Moulton method [15] is implemented.

Predictor:

$$\mathbf{y_p} = \mathbf{y_p} + \frac{dt}{24}(55\mathbf{V_n} - 59\mathbf{V_{n-1}} + 37\mathbf{V_{n-2}} - 9\mathbf{V_{n-3}}) \tag{18}$$

Corrector:

$$\mathbf{y_{n+1}} = \mathbf{y_n} + \frac{dt}{24}(9\mathbf{V_p} - 19\mathbf{V_{n-1}} + 5\mathbf{V_{n-1}} + \mathbf{V_{n-2}}) \tag{19}$$

where $\mathbf{y_p}$ is the position at an intermediate step. This predictor–corrector method is known to be more stable than the conventional explicit method for the wake roll-up.

D. Discretization of the BIF

To numerically solve the BIF expressed in Eq. (9), the body surface is discretized into a set of quadrilateral panels, and a potential distribution with a constant strength is assumed on each panel. Body surfaces are modeled by M elements, and each panel of the body surface is required to satisfy the BIF at collocation points placed at the center of the panel. The wake surfaces are divided by N elements. Then, for each panel, the discretized form for an unsteady flow becomes

$$E_k(t)\phi_k(t) = \sum_{m=1}^{M} B_{km}(t)\chi_{km}(t) + \sum_{m=1}^{M} C_{km}(t)\phi_{km}(t) + \sum_{n=1}^{N} F_{kn}(t)\Delta\phi_{kn}(t) \tag{20}$$

where $E_k(t) = E(x_k, t) = 0$, $\chi_m = (\partial\phi/\partial n)_m$,

$$B_{km} = \int_{s_m} \frac{-1}{4\pi|x - x_k|}\mathrm{d}s \tag{21}$$

$$C_{km} = \int_{s_m} \frac{\partial}{\partial n}\left(\frac{1}{4\pi|x - x_k|}\right)\mathrm{d}s \tag{22}$$

$$F_{km} = \int_{s_m} \frac{\partial}{\partial n}\left(\frac{1}{4\pi|x - x_k|}\right)\mathrm{d}s \tag{23}$$

The coefficients B_{km} and C_{km}, which are the body surface contributions, are time-independent if the surface S_B moves in a rigid-body motion, but the wake contribution F_{kn} is time-dependent in unsteady flows. Hence, this term should be updated at every time step. At each time step, χ_{km} is known from the boundary condition, and $\Delta\phi$ is also known from the Kutta condition and the preceding time steps. Finally, the solution of Eq. (20) yields ϕ_k on the blade surface. Equations (21–23) can be solved by analytic formulations given by Hess and Smith [16] for a constant strength of the potential distribution on each panel.

E. Bernoulli Equation for an Unsteady Panel Method

Pressure on the blade surfaces can be computed using the velocity potential and flow velocity.

Unsteady Bernoulli equation:

$$\frac{\partial\phi}{\partial t} + \frac{1}{2}\mathbf{v}^2 + \frac{1}{\rho}p = \frac{1}{\rho}p_{\mathrm{ref}} \tag{24}$$

The nondimensionalized form of the pressure is given as

$$C_p = \frac{p - p_{\mathrm{ref}}}{1/2\rho\mathbf{v_{ref}^2}} = 1 - \frac{\mathbf{v^2}}{\mathbf{v_{ref}^2}} - \frac{2}{\mathbf{v_{ref}^2}}\frac{\partial\phi}{\partial t} \tag{25}$$

where $\mathbf{v}$ and p are the local fluid velocity and pressure, respectively. The time derivative of the potential in Eq. (25) is evaluated with second-order backward differentiation in the present work. Reference pressure p_{ref} is the far-field reference pressure and $\mathbf{v_{ref}}$ can be selected as the kinematic velocity:

$$\mathbf{v_{ref}} = -[\mathbf{V_0} + \Omega \times \mathbf{r}] \tag{26}$$

where $\mathbf{V_0}$ is the flight velocity of a vehicle in a ground-fixed frame, Ω is the angular velocity, and $\mathbf{r}$ is the relative position from the reference frame.

Finally, the aerodynamic force can be computed as

$$\Delta F_k = -C_{Pk}(\tfrac{1}{2}\rho v_{\mathrm{ref}}^2)_k \Delta A_k n_k \tag{27}$$

where ΔF_k is the aerodynamic loads on the panel, for which the area is denoted by ΔA_k.

F. Instability of the Initial Wake

If the rotor is rotated with sudden acceleration, the initial wake will have unstable behavior. To reduce the instability of the initial wake, Chung et al. [7] presented a slow starting method whereby the nonphysical unstable behavior of the initial wake is suppressed by decreasing the vortical strength of the starting vortex. This method is applied to the present free-wake method. The rotational speed is assumed to increase slowly from zero to the desired value over one or two revolutions. Slow starting over one or two revolutions can provide a more accurate and stable numerical solution.

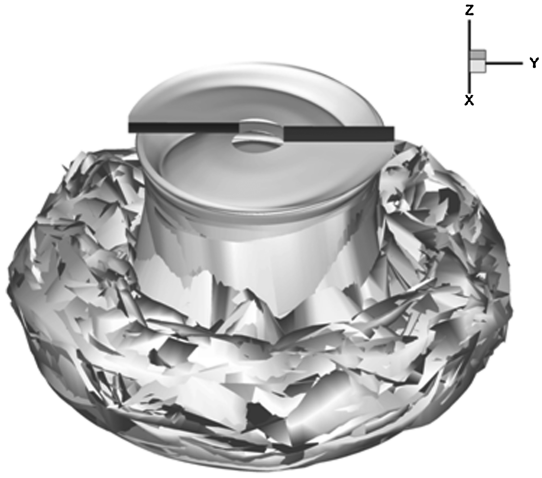

Fig. 5 Rotor wake geometry in hover.

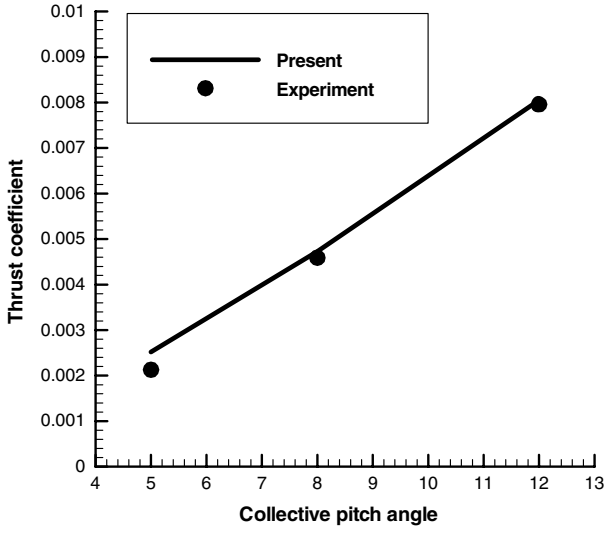

Fig. 6 Total thrust coefficient.

V. Numerical Results

In this section, lifting helicopter rotor blades in hover, vertical, and forward flights are considered. In particular, tip-vortex pairing phenomena in vertical flight are investigated after 30 revolutions. It is difficult to accurately predict the tip-vortex positions due to the complexity of wake convection. After simulation of hovering and vertical flight cases, forwarding-flight rotors with pitching and flapping blade motions are analyzed. All of the numerical results are compared with available experimental data such as thrust coefficient, pressure coefficients, and tip-vortex trajectories.

A. Helicopter Rotor in Hover Flight

Caradonna and Tung's [17] two-blade rotor experiment is analyzed for a hovering rotor. The rotor radius is 1.143 m and the aspect ratio is 6. This blade is not tapered and not twisted. The

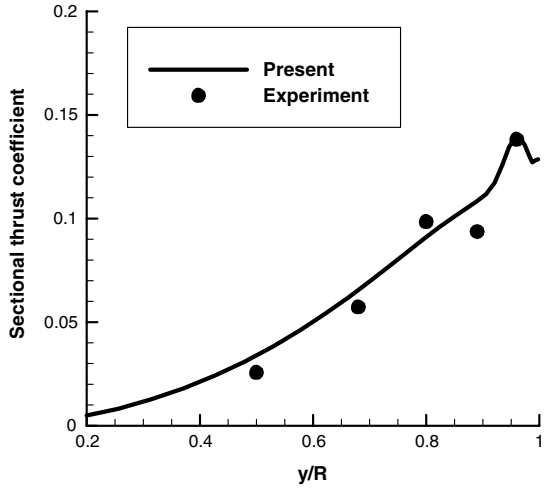

a) Pitch angle=5 deg

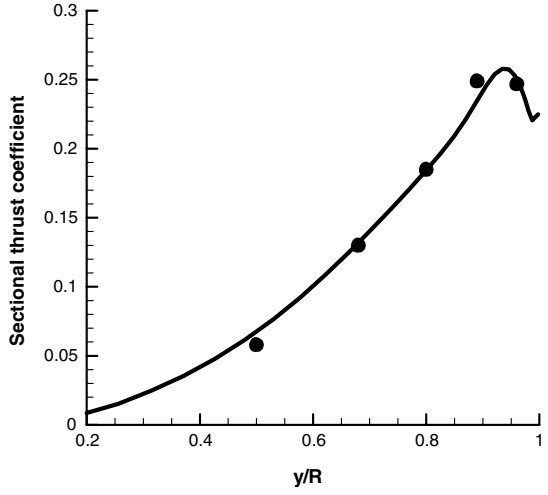

b) Pitch angle=8 deg

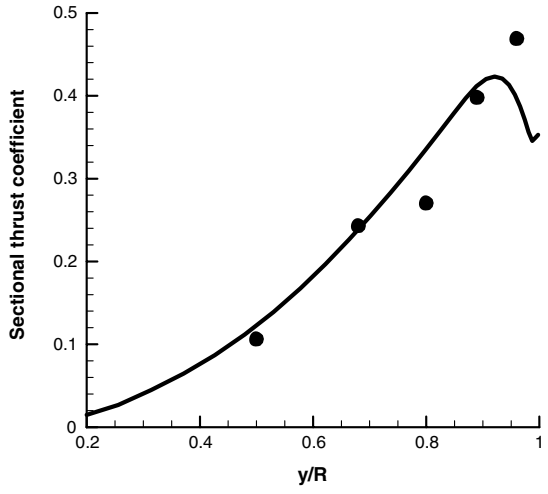

c) Pitch angle=12 deg

Fig. 7 Sectional thrust coefficient.

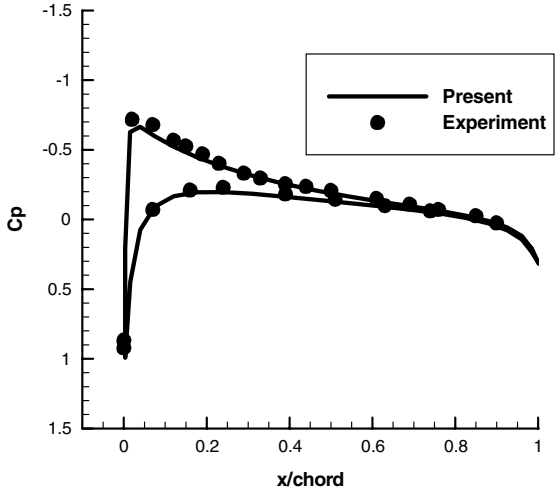

a) r/R=0.96

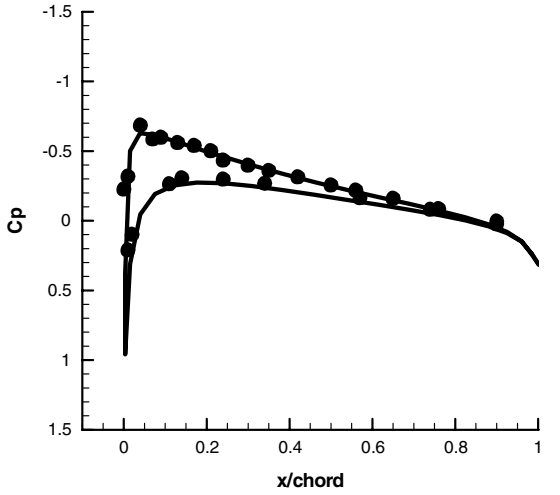

b) r/R=0.8

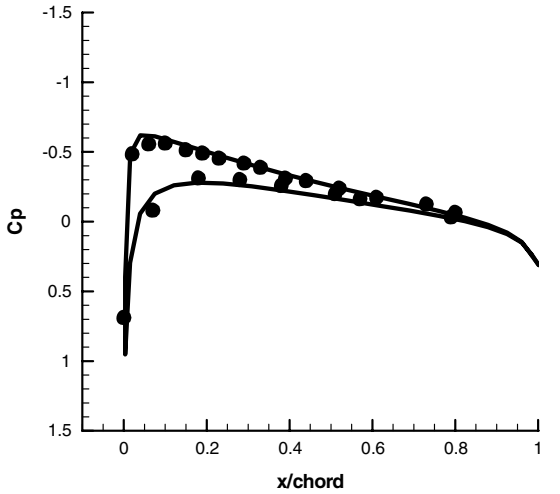

c) r/R=0.68

Fig. 8 Pressure coefficient at a collective pitch angle of 5 deg.

sectional airfoil is NACA0012. The root cutout is approximately equal to one chord. The pressure taps are located at specific spanwise locations, with more data being taken near the tip and near the leading edge. The case presented in this paper involves a rotor with 5, 8, and 12 deg of collective pitch angle, rotating at 1250 rpm, which corresponds to a tip Mach number equal to 0.439.

The computational model is composed of 40 panels in the chordwise direction and 30 panels in the spanwise direction, respectively, on each blade. Panel clustering is given in close proximity to the blade tip region and the leading edge of the blade. Computational results for the current case have been obtained with an azimuthal step of 15 deg. These hovering cases are performed over 10 revolutions; 15 CPUs (Intel core 2, 2.4 GHz) are used for parallel computation, and the total computational time is about 35 min.

Figure 5 shows the rotor wake geometry in hover. Wake contraction near the rotor plane and bundle region far below the plane is well captured. In Fig. 6, the total thrust coefficients are compared with experimental data at collective pitch angles of 5, 8, and 12 deg.

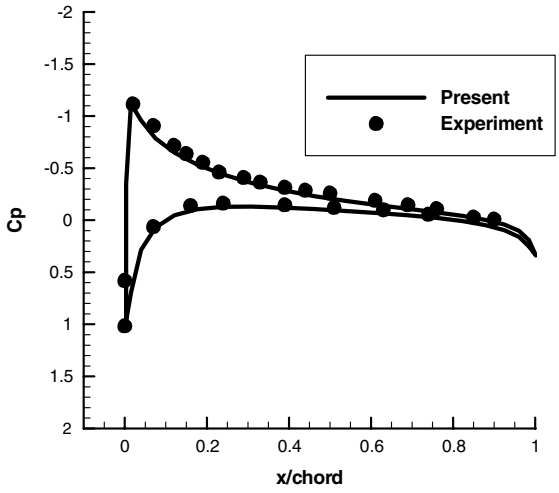

a) r/R=0.96

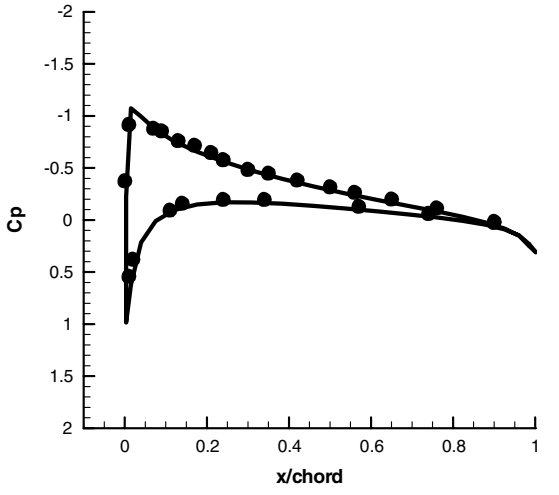

b) r/R=0.8

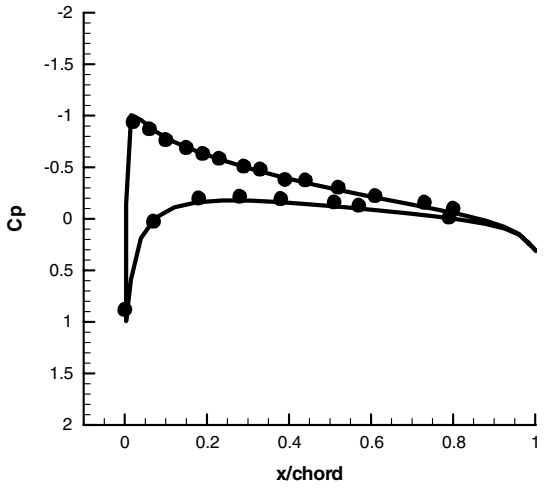

c) r/R=0.68

Fig. 9 Pressure coefficients at a collective pitch angle of 8 deg.

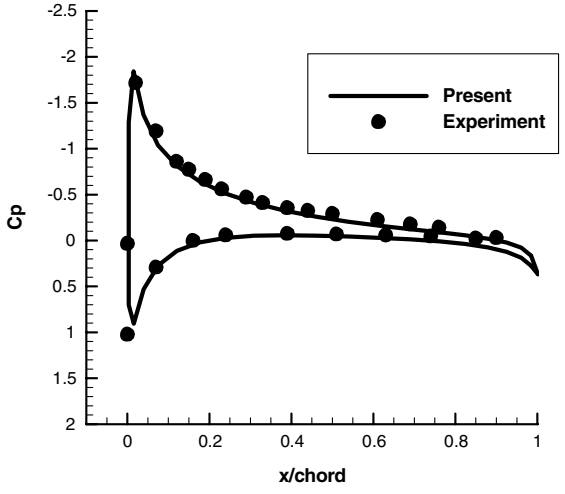

a) r/R=0.96

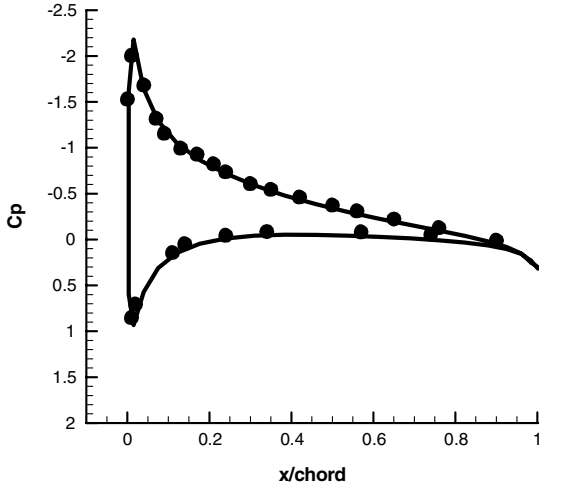

b) r/R=0.8

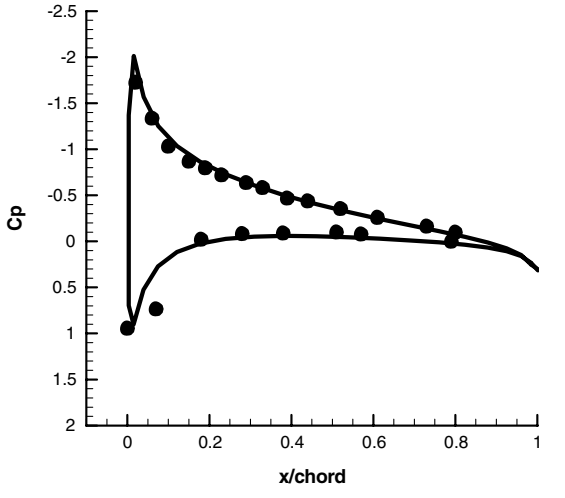

c) r/R=0.68

Fig. 10 Pressure coefficients at a collective pitch angle of 12 deg.

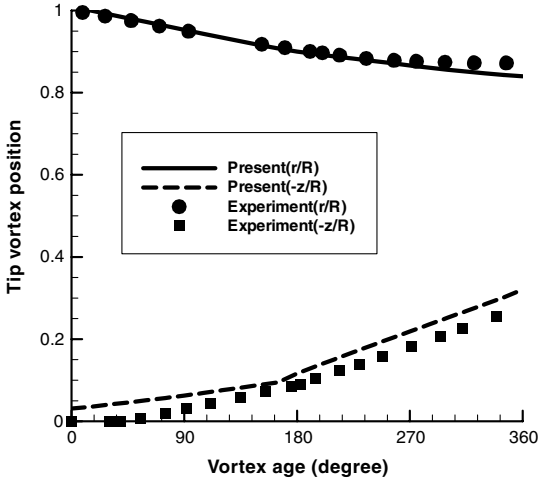

Fig. 11 Tip-vortex positions at a collective pitch angle of 8 deg.

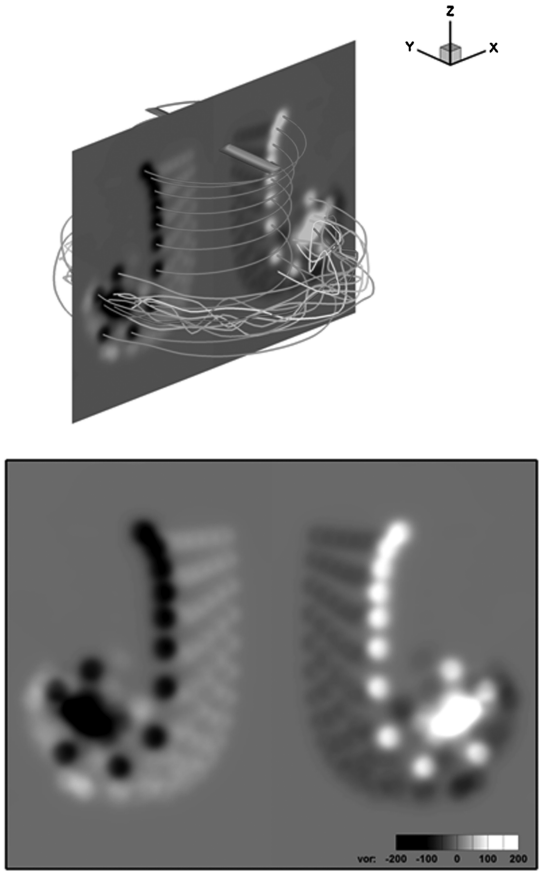

Fig. 12 Vorticity contour in the cross section.

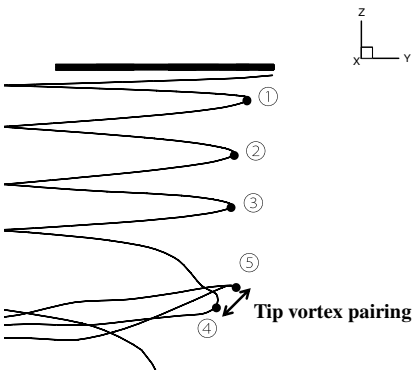

Fig. 13 Sectional view of the predicted tip vortex.

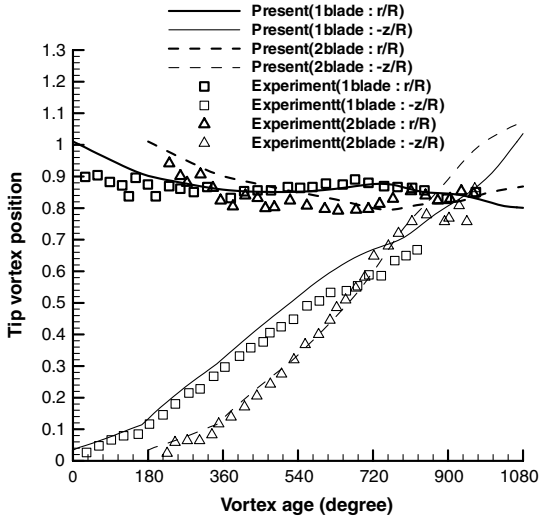

Fig. 14 Tip-vortex pairing position of the AH-1G model (pitch angle is 11 deg and climb rate is 1.067 m/s).

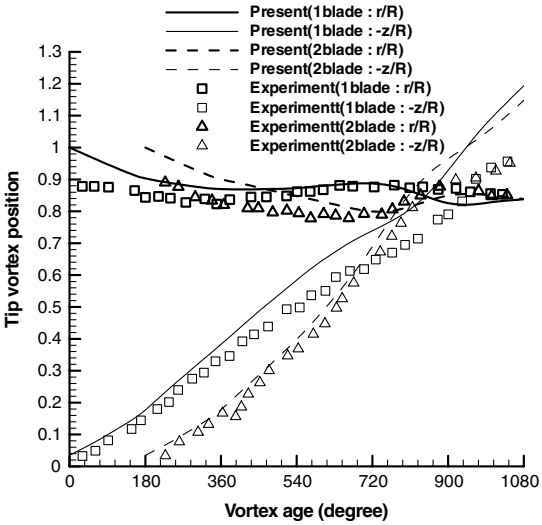

Fig. 15 Tip-vortex pairing position of the AH-1G model (pitch angle is 11 deg and climb rate is 2.928 m/s).

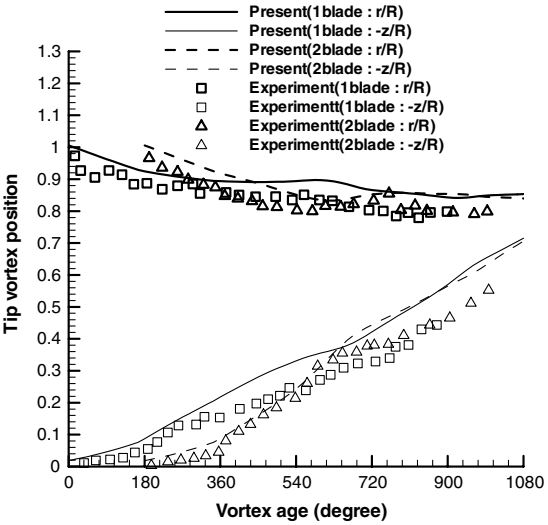

Fig. 16 Tip-vortex pairing position of the AH-1G model (pitch angle is 6 deg and climb rate is 1.067 m/s).

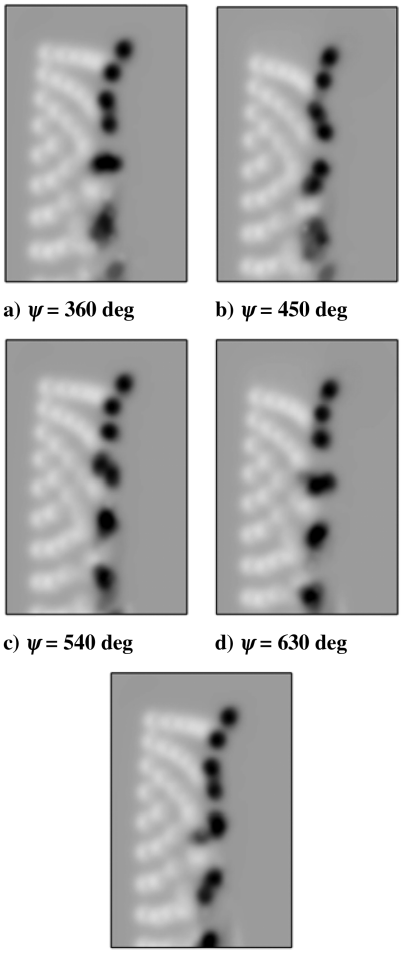

Fig. 17 Vorticity contour of tip-vortex pairing (ψ: vortex age) (pitch angle is 11 deg and climb rate is 1.067 m/s).

At the high pitch angle as well as the low pitch angle, the predicted thrust coefficients are in very good agreement with the experimental results.

The variation of the sectional thrust along the blade span is displayed in Fig. 7. Experimental data are compared with predicted results. Most of predicted results have a good agreement with experimental data. But the results of a pitch angle of 12 deg have little difference at outer region of the blade, because with the present method, it is difficult to describe the airload variation of leading-edge separation at a high pitch angle.

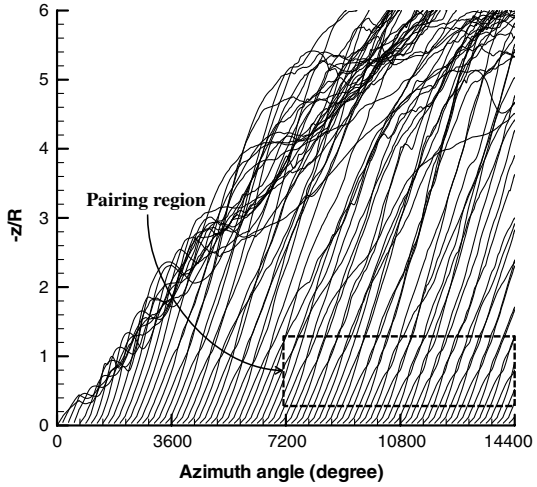

Fig. 18 tip-vortex geometry during 40 revolutions (pitch angle is 11 deg and climb rate is 1.067 m/s).

Table 1 Cyclic control angle of AH-1G

unit: degree	θ_0	θ_{1s}	θ_{1c}	β_{1s}	β_{1c}
Present prediction (after trim)	6.02	−3.26	1.55	−0.15	2.13
Experiment	6	−5.5	1.7	−0.15	2.13

Table 2 Thrust and moment coefficients

	C_T	C_{Mx}	C_{My}
Present prediction (after trim)	0.00464	-6.5×10^{-6}	-5.2×10^{-7}
Experiment	0.00464	0	0

Figures 8–10 show the pressure coefficient at three blade-span sections ($r/R = 0.96, 0.8, 0.68$). The numerical results are in fairly good agreement with the experimental results for all regions. The present method accurately predicts aerodynamics of the helicopter rotor in hover at the given collective pitch angle.

B. Tip-Vortex Descriptions

Caradonna and Tung's [17] rotor model is used for the simple tip-vortex movement calculation. This model has a pitch angle of 8 deg and is performed for 10 revolutions. Figure 11 shows a tip-vortex position in both the radial direction (r/R) and axial direction ($-z/R$) as a function of the vortex age. The converged tip trajectory obtained from the 10th revolution was used. Experimental data were included in the figure for the comparison. It can be seen that the radial contraction of the wake agrees very well with the measured data, whereas the downward convection of the wake is slightly over-predicted, compared with the measurement.

Figure 12 illustrates the vorticity contour in a sectional plane normal to the rotor plane after 10 revolutions. It is shown that the strong tip vortices and weak inboard vortices were captured very well.

For the complicated tip-vortex pairing simulation, the subscale AH-1G model [18] is simulated. The AH-1G model with a radius of 1.0414 m rotates at 1800 rpm. This model has a climb rate of 1.067 m/s, with 2.928 m/s in the axial direction. During 80 revolutions, this model is performed at a collective pitch angle of 11 deg. The blade is composed of 40 chordwise panels and 12 spanwise panels. The pairing case has been obtained with an azimuthal step of 15 deg; 12 CPUs are used for parallel computation and the total computational time is about 29 h.

The predicted tip-vortex positions of AH-1G are shown in Figs. 13–16. Figure 13 indicates the predicted tip-vortex geometry in the cross section. In this figure, the fourth vortex is pared with the fifth vortex. Tip-vortex pairing progresses until their positions interchange. In Figs. 14–16, the tip-vortex pairing position is shown quantitatively. The radial r/R and axial $-z/R$ positions of the tip

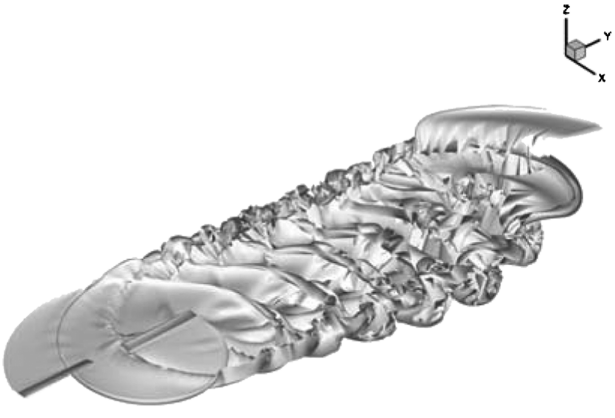

Fig. 19 Rotor wake geometry in forward flight.

vortex at the 30th–33rd revolutions are displayed. Their positions have a 180 deg phase shift because of the two blades. These predicted results correlate well with experimental data. Figure 17 shows a vorticity contour in a sectional plane. In this figure, tip-vortex pairing is visualized with vortex age. At a vortex age (reference azimuth) of 360–720 deg, two tip-vortex trajectories cross due to the interchange of pairing. Figure 18 shows all tip-vortex trajectories during 40 revolutions. In this figure, it is shown that convergence of the tip-vortex pairing position is initiated at an azimuth angle of 7200 deg (20th revolution), demonstrating that the numerical simulation requires many revolutions of the rotating blades to capture the detailed behavior of the wake dynamics.

C. Helicopter Rotor in Forward Flight

For a forwarding simulation, the AH-1G model [19] is simulated. The aspect ratio of the rotor blade is 9.8 and the linear twist rate is −10 deg from root to tip. The rotor is operated at a tip Mach number of 0.65 and an advance ratio of 0.19. The computational blade model is composed of 40 chordwise and 16 spanwise panels. An azimuthal angle step is $\Delta\psi = 3$ deg. The computational time to run 4 revolutions took about 8 h with 16 CPUs for the current case.

The AH-1G model has two blades with periodic pitching and flapping motions. Pitching and flapping motions are described by a sinusoidal function of azimuth angle ψ.

Pitch angle:

$$\theta(\psi) = \theta_0 + \theta_{1c}\cos(\psi) + \theta_{1s}\sin(\psi) + \cdots \tag{28}$$

Flapping angle:

$$\beta(\psi) = \beta_0 + \beta_{1c}\cos(\psi) + \beta_{1s}\sin(\psi) + \cdots \tag{29}$$

where θ and β represent the pitch and flap angles, respectively. Blade motion coefficients are determined through the flight trim process.

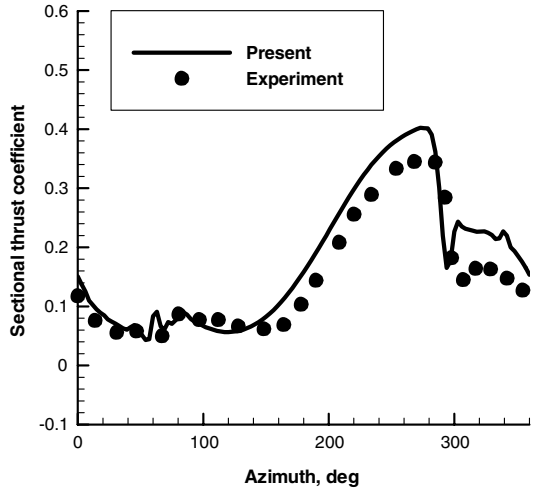

a) r/R=0.97

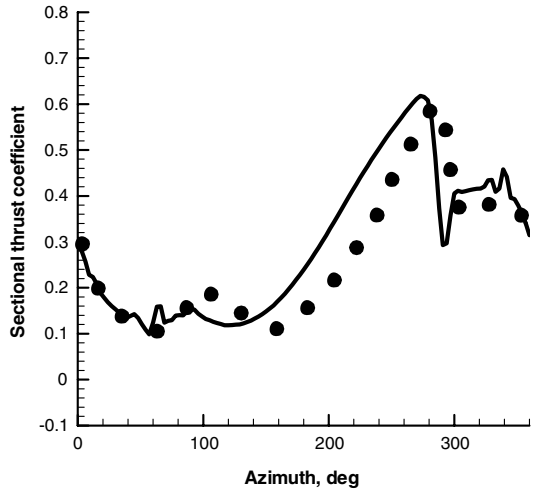

b) r/R=0.91

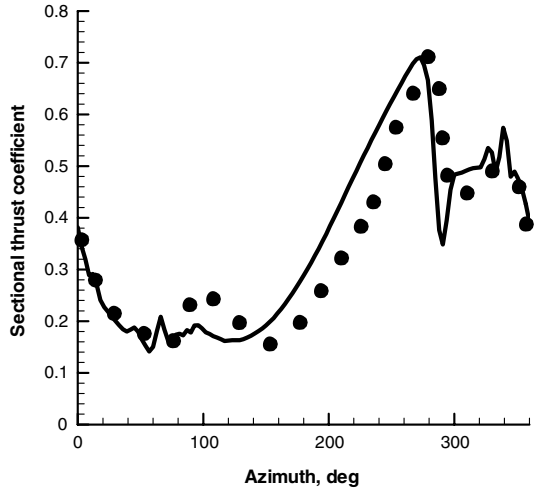

c) r/R=0.87

Fig. 20 Sectional thrust coefficients with azimuth variation.

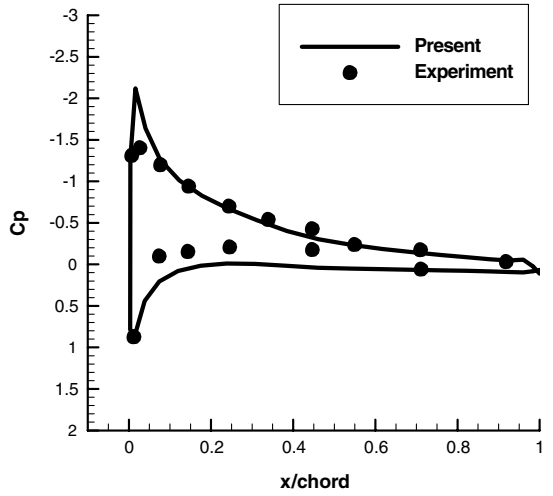

a) Azimuth=30 deg

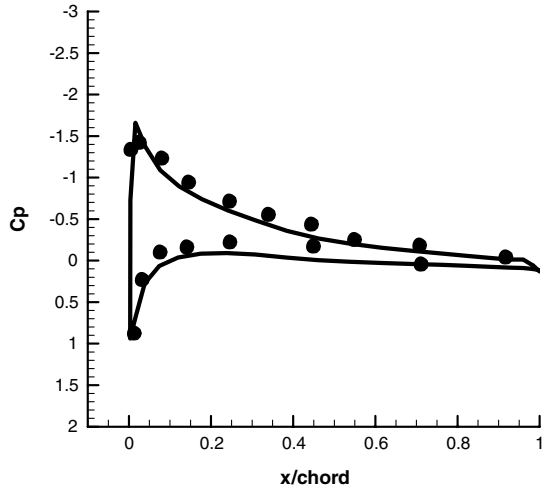

b) Azimuth=90 deg

Fig. 21 Pressure coefficient at $r/R = 0.6$.

By varying cyclic pitch-angle coefficients ($\theta_0, \theta_{1c}, \theta_{1s}$), thrust and moment can be converged to the desired level:

$$C_T = C_T(\theta_0, \theta_{1c}, \theta_{1s}) \qquad C_{Mx} = C_{Mx}(\theta_0, \theta_{1c}, \theta_{1s})$$
$$C_{My} = C_{My}(\theta_0, \theta_{1c}, \theta_{1s}) \tag{30}$$

where the subscripts x and y denote the x and y coordinates of the rotational plane x–y.

$$\begin{bmatrix} \Delta\theta_0 \\ \Delta\theta_{1c} \\ \Delta\theta_{1s} \end{bmatrix} = \begin{bmatrix} \frac{\partial C_T}{\partial\theta_0} & \frac{\partial C_T}{\partial\theta_{1c}} & \frac{\partial C_T}{\partial\theta_{1s}} \\ \frac{\partial C_{Mx}}{\partial\theta_0} & \frac{\partial C_{Mx}}{\partial\theta_{1c}} & \frac{\partial C_{Mx}}{\partial\theta_{1s}} \\ \frac{\partial C_{My}}{\partial\theta_0} & \frac{\partial C_{My}}{\partial\theta_{1c}} & \frac{\partial C_{My}}{\partial\theta_{1s}} \end{bmatrix}^{-1} \begin{bmatrix} \Delta C_T \\ \Delta C_{Mx} \\ \Delta C_{My} \end{bmatrix} \tag{31}$$

where ΔC_T, ΔC_{Mx}, and ΔC_{My} are differences between the desired valued and the computed value. Equation (31) indicates the algebraic relation between the aerodynamic properties and control angles. The Newton–Raphson iterative method is used for iteration of the pitch-angle coefficients. After this convergence process, cyclic pitch-angle coefficients are determined for simulation of forward flight.

Table 1 shows the cyclic pitch angle after the trim procedure. Table 2 indicates the predicted thrust and moment coefficients. In Table 2, the predicted trim results and experimental data are almost the same. Figure 19 shows the rotor wake calculated by the present unsteady panel method. In this figure, the wake roll-up at the blade tip

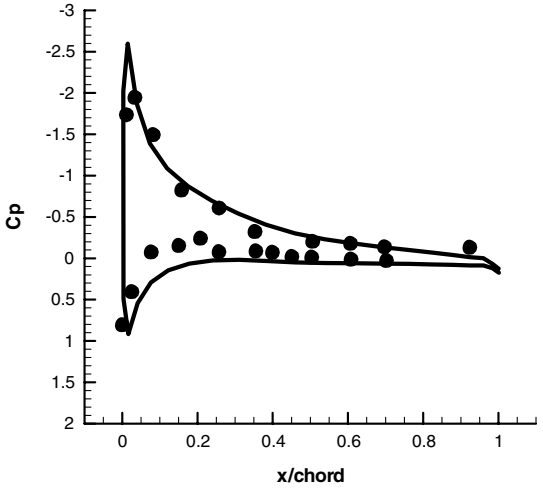

a) Azimuth=270 deg

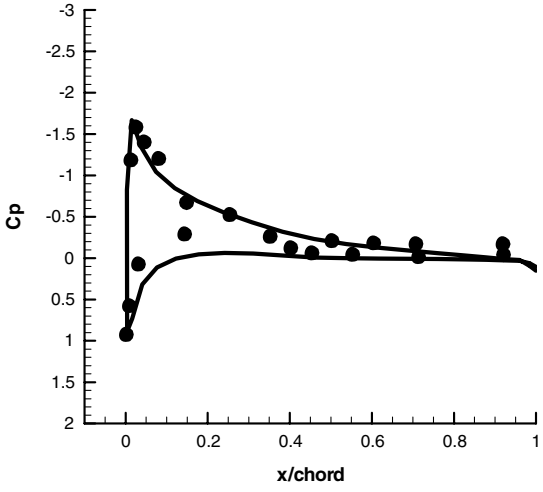

b) Azimuth=300 deg

Fig. 22 Pressure coefficient at $r/R = 0.91$.

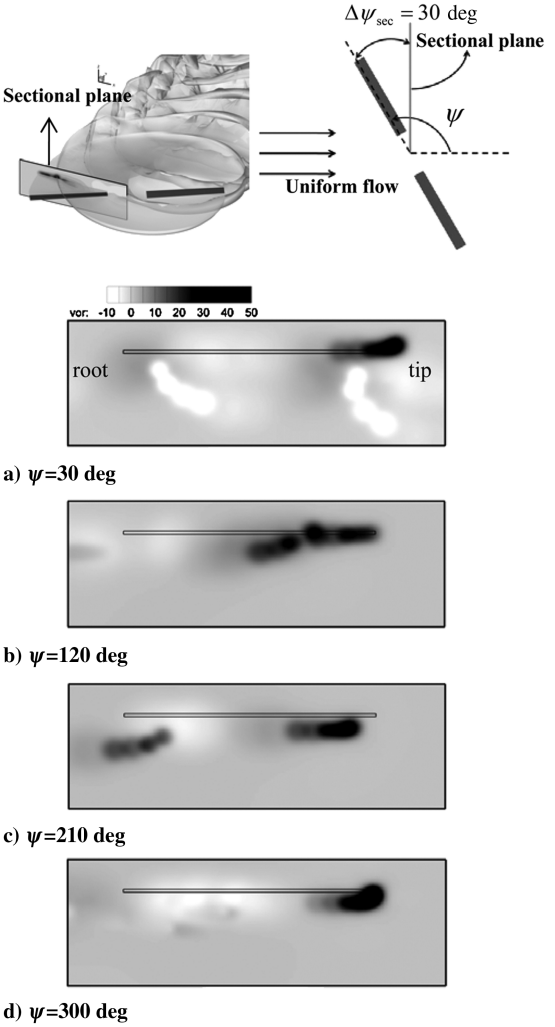

a) ψ=30 deg

b) ψ=120 deg

c) ψ=210 deg

d) ψ=300 deg

Fig. 23 Vorticity contour of the rotational section in forward flight.

is captured well and wake convection is also observed. Figure 20 illustrates the variation of the sectional thrust coefficient at selected spanwise positions over one revolution. Figures 21 and 22 show the pressure coefficient at specific span positions ($r/R = 0.6, 0.91$) at azimuth angles of 30, 90, 270, and 300 deg. It is shown that the predicted results agree well with the measured data. Figure 23 shows the vorticity contour in the rotational sectional plane. To investigate the trailing vortex strength, the sectional plane also rotates. The vortex strength is plotted at a plane of 30 deg after the blade. The position and strength of the tip vortex at the specific azimuth angle were clearly captured. The inboard wake vorticity variation was also observed. In this figure, we can confirm that the inboard wake strength variation as well as the tip vortex are investigated. Figure 24 also presents a vorticity contour of a sectional plane in the flight direction. These sections are located at specific positions (R, $2R$, $3R$, and $4R$). In Fig. 24, it is shown that the wake is distorted in each section. The figures show the movement of the tip and inboard wake during forward flight.

VI. Conclusions

A potential-based doublet panel method coupled with a free-wake method is proposed to predict the unsteady aerodynamics and wake dynamics in a rotorcraft application. The doublet panel method and the advanced time-marching free-wake method are tightly coupled using the equivalence between the doublet potential wake panels and vortex filaments. The respective advantages of both methods are maintained in the present method. The doublet panel method provides a detailed pressure distribution along the chord, and the

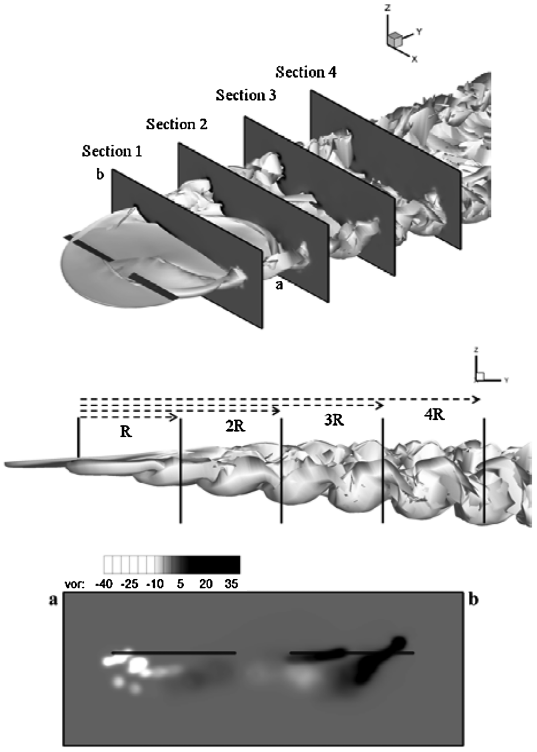

a) Section 1: R

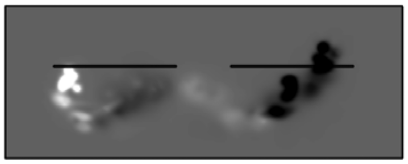

b) Section 2: 2R

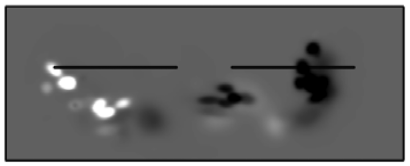

c) Section 3: 3R

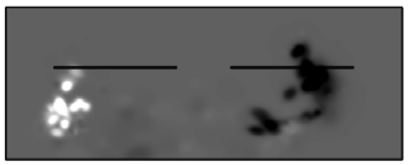

d) Section 4: 4R

Fig. 24 Vorticity contour of the fixed section in forward flight.

free-wake method provides accurate modeling of the wake dynamics.

The present coupled method was applied to a helicopter rotor in both hovering and forward flights. It was shown that the predicted airloads agree very well with measured data. The wake dynamics was analyzed in detail by investigating the tip-vortex trajectory in the radial and axial directions, as well as the tip-vortex pairing phenomena. The tip-vortex pairing was first captured in the unsteady panel method. Parallel processing was implemented such that the induced velocity computation from each vortex filament is separately calculated.

It should be noted that the current potential method fails to address flow compressibility such as shock around the blades with high tip Mach number, dynamic flow separation, and turbulence effects, although the viscosity effect can be modeled if a boundary-layer formulation is correlated with the current method. Those effects, however, are known to not play a significant role in determining wake dynamics. In addition, the method can be used to design advanced blade platform shapes or rotors with high twist for high performance with high accuracy and less intensive computational effort.

Acknowledgments

This work was supported by the Defense Acquisition Program Administration (South Korea), the Korean Agency for Defense Development under contract UD070041 AD, and the Korea Aerospace Research Institute (KARI) and Korea Helicopter Program (KHP) Dual-Use Component Development Program funded by the Ministry of Commerce, Industry and Energy (MOCIE).

References

[1] Richason, T. F., and Katz, J., "Unsteady Panel Method for Flows with Multiple Bodies Moving Along Various Paths," *AIAA Journal*, Vol. 32, No. 1, 1994, pp. 62–68. doi:10.2514/3.11951

[2] Katz, J., and Maskew, B., "Unsteady Low-Speed Aerodynamic Model for Complete Aircraft Configurations," *Journal of Aircraft*, Vol. 25, No. 4, 1988, pp. 302–310. doi:10.2514/3.45564

[3] Morino, L., and Kuo, C., "Subsonic Potential Aerodynamics for Complex Configuration," *AIAA Journal*, Vol. 12, No. 2, 1974, pp. 191–197. doi:10.2514/3.49191

[4] Morino, L., Bharadvaj, B. K., Freedman, M. I., and Tseng, K., "Boundary Integral Equation for Wave Equation with Moving Boundary and Applications to Compressible Potential Aerodynamics of Airplanes and Helicopter," *Computational Mechanics*, Vol. 4, No. 4, 1989, pp. 231–243. doi:10.1007/BF00301382

[5] Bagai, A., and Leishman, J. G., "Rotor Free-Wake Modeling Using a Relaxation Technique Including Comparisons with Experimental Data," *Journal of the American Helicopter Society*, Vol. 40, No. 3, 1995, pp. 29–41.

[6] Bagai, A., and Leishman, J. G., "Rotor Free-Wake Modeling Using a Pseudoimplicit Relaxation Algorithm," *Journal of Aircraft*, Vol. 32, No. 6, Dec. 1995, pp. 1276–1285. doi:10.2514/3.46875

[7] Chung, K. H., Kim, J. W., Ryu, K. W., Lee, K. T., and Lee, D. J., "Sound Generation and Radiation from Rotor Tip-Vortex Pairing Phenomenon," *AIAA Journal*, Vol. 44, No. 6, 2006, pp. 1181–1187. doi:10.2514/1.22548

[8] Ahmed, S., and Vidjaja, V. T., "Unsteady Panel Method Calculation of Pressure Distribution on BO 105 Model Rotor Blades," *Journal of the American Helicopter Society*, Vol. 43, No. 1, 1998, pp. 47–56.

[9] Morino, L., "Boundary Integral Equations in Aerodynamics," *Applied Mechanics Reviews*, Vol. 46, No. 8, 1993, pp. 445–466.

[10] Ryu, K. H., and Lee, D. J., "Interaction Between a Vortex Ring and a Rigid Sphere," *European Journal of Fluid Mechanics—Fluids Series*, Vol. 16, No. 5, 1997, pp. 654–664.

[11] Leishman, J. G., Baker, A., and Coyne, A. J., "Measurements of Rotor Tip Vortices Using Three-Component Laser Doppler Velocimetry," *Journal of the American Helicopter Society*, Vol. 41, No. 4, Oct. 1996, pp. 342–345.

[12] Gennaretti, M., and Bernardini, G., "Novel Boundary Integral Formulation for Blade-Vortex Interaction Aerodynamics of Helicopter Rotors," *AIAA Journal*, Vol. 45, No. 6, June 2007, pp. 1169–1176. doi:10.2514/1.18383

[13] Scully, M. P., "Computation of Helicopter Rotor Wake Geometry and Its Influence on Rotor Harmonic Airloads," Massachusetts Inst. of Technology, Rept. ASRL TR 178-1, Cambridge, MA, 1975.

[14] Vatistas, G. H., Kozel, V., and Mih, W. C., "A Simpler Model for Concentrated Vortices," *Experiments in Fluids*, Vol. 11, No. 1, 1991, pp. 73–76. doi:10.1007/BF00198434

[15] Cheney, W., and Kincaid, D., "Adams-Bashforth-Moulton Methods," *Numerical Mathematics and Computing*, 5th ed., Thomson Science, London, 2004, pp. 508–518.

[16] Hess, J., and Smith, A. M. O., "Calculation of Non-Lifting Potential Flow about Arbitrary Three-Dimensional Bodies," *Journal of Ship Research*, Vol. 8, No. 2, 1964, pp. 22–44.

[17] Caradonna, F. X., and Tung, C., "Experimental and Analytical Studies of a Model Helicopter Rotor in Hover," NASA TM-81232, 1982.

[18] Caradonna, F., Hendley, E., Silva, M., Huang, S., Komerath, N., Reddy, U., Mahalingam, R., Funk, R., Ames, R., Darden, L., Villareal, L., Gregory, J., and Wong, O., "An Experimental Study of a Rotor In Axial Flight," *AHS Specialists' Meeting on Aerodynamics and Aeroacoustics*, AHS International, Alexandria, VA, Oct. 1997.

[19] Cross, J. L., and Watts, M. E., "Tip Aerodynamics and Acoustics Test: A Report and Data Survey," NASA Ames Research Center Rept. NASA-RP-1179, Moffett Field, CA, Dec. 1988.